



# Volume-based, layer-independent, disease-agnostic detection of abnormal retinal reflectivity, nonperfusion, and neovascularization using structural and angiographic OCT

SHAOHUA PI,<sup>1</sup> TRISTAN T. HORMEL,<sup>1</sup> BINGJIE WANG,<sup>1</sup> STEVEN T. BAILEY,<sup>1</sup> THOMAS S. HWANG,<sup>1</sup> DAVID HUANG,<sup>1</sup> JOHN C. MORRISON,<sup>1</sup> AND YALI JIA<sup>1\*</sup>

*Casey Eye Institute, Oregon Health & Science University, Portland, OR, USA*

\*jiaya@ohsu.edu

**Abstract:** Optical coherence tomography (OCT) is widely used in ophthalmic practice because it can visualize retinal structure and vasculature *in vivo* and 3-dimensionally (3D). Even though OCT procedures yield data volumes, clinicians typically interpret the 3D images using two-dimensional (2D) data subsets, such as cross-sectional scans or *en face* projections. Since a single OCT volume can contain hundreds of cross-sections (each of which must be processed with retinal layer segmentation to produce *en face* images), a thorough manual analysis of the complete OCT volume can be prohibitively time-consuming. Furthermore, 2D reductions of the full OCT volume may obscure relationships between disease progression and the (volumetric) location of pathology within the retina and can be prone to mis-segmentation artifacts. In this work, we propose a novel framework that can detect several retinal pathologies in three dimensions using structural and angiographic OCT. Our framework operates by detecting deviations in reflectance, angiography, and simulated perfusion from a percent depth normalized standard retina created by merging and averaging scans from healthy subjects. We show that these deviations from the standard retina can highlight multiple key features, while the depth normalization obviates the need to segment several retinal layers. We also construct a composite pathology index that measures average deviation from the standard retina in several categories (hypo- and hyper-reflectance, nonperfusion, presence of choroidal neovascularization, and thickness change) and show that this index correlates with DR severity. Requiring minimal retinal layer segmentation and being fully automated, this 3D framework has a strong potential to be integrated into commercial OCT systems and to benefit ophthalmology research and clinical care.

© 2022 Optica Publishing Group under the terms of the [Optica Open Access Publishing Agreement](#)

## 1. Introduction

The human retina is a light-sensitive tissue located between the vitreous and the choroid [1], and the retinal pathologies can occur anywhere throughout the complex, layered structure. The most prevalent clinical imaging modality for evaluating the retina is optical coherence tomography (OCT), due to its three-dimensional (3D), non-invasive nature, and micron-scale resolution [2–4]. As a functional extension of OCT, OCT angiography (OCTA), when combined with structural OCT, enables simultaneous visualization of retinal structure and vascular morphology without requiring intravenous dye for contrast [5–7]. Using structural OCT and OCTA, highly-organized laminar layers spanning the entire retina from the inner limiting membrane (ILM) to Bruch's membrane (BM) [8], the avascular foveal pit in the macula [9], and vascular plexuses supplying specific anatomic slabs [10] can all be observed simultaneously in a data volume obtained from a single scan. Structural OCT and OCTA measurements (e.g., layer thicknesses [11],

neovascularization [12], nonperfusion areas [6], or vessel densities) can be extracted through post-processing and used for disease diagnosis [13].

Although structural OCT and OCTA provide volumetric data, both human graders and algorithms usually analyze cross-sections or *en face* images constructed by projecting the OCT/OCTA signals across a retinal slab. Analytic approaches that rely on 2D reductions of the full 3D data volume incur some disadvantages, such as the requisite anatomic layer segmentation to create *en face* images [14,15] and the potential for 2D representations to distort the important qualities of some features that are best captured in 3D. On the other hand, a full 3D characterization of structural (e.g. retinal fluid volume [16]) and vascular pathologies (e.g. 3D parafoveal vessel density [17]) is more sensitive for classifying and staging diseases than the same biomarkers characterized only in 2D. Nonetheless, volumetric characterization of pathology remains under-utilized, which is in part due to the difficulty of visualizing and analyzing 3D data.

To address this issue, we developed a conceptually simple framework that can readily detect retinal pathologies and visualize its locations in 3D. This framework relies on comparing target scans to a standard retina volume constructed by averaging scans from several healthy retinas. Volumetric registration, merging, and comparison of macular scans from different subjects were achieved by normalizing to percent depth within the retina and laterally aligning foveal avascular zones (FAZ). This process requires segmentation of just two anatomic layer boundaries (ILM and BM), which can be compared to the many OCT algorithms that require segmentation of several anatomic layers [15]. Our method also smooths out variations between individual healthy retinas, such as differences in retinal thickness [18] and curvature [19]. Then, when an OCT scan reveals a large deviation compared to the standard retina, it is likely to correspond to a pathologic feature. We show that a wide spectrum of clinical features, such as paracentral acute middle maculopathy (PAMM), drusen, retinal fluid, neovascularization, and nonperfusion can be detected and visualized in this way. In addition, we construct a novel pathology index that measures the average deviation of a retinal volume from the standard and show that this index correlates with DR severity. Our framework has potential as both a visual/interpretive aid and a foundation for quantitative analysis.

## 2. Methods

### 2.1. OCT and OCTA scans

Participants in this study were enrolled with written consent in accordance with an Institutional Review Board/Ethics Committee approved protocol at the Oregon Health & Science University and in accordance with the Declaration of Helsinki and compliant with the Health Insurance Portability and Accountability Act of 1996. As shown in Table 1, healthy control participants ( $n = 48$ , 6×6-mm scan), participants with diabetes ( $n = 325$ , including 55 healthy subjects), retinal artery occlusion (RAO,  $n = 19$ ), and age-related macular degeneration (AMD,  $n = 142$ , including both dry-AMD and wet-AMD) were included in this study. The age of subjects covered a wide range, and the gender ratio was about half and half (M: 47.7%, F: 52.3%). All participants underwent a complete ophthalmic examination. However, information such as visual acuity, axial length, weight, blood pressure, IOP, and treatment history was unavailable for all subjects and therefore was not included. For patients with diabetes, an Early Treatment of Diabetic Retinopathy Study (ETDRS) score [20] was used to classify the severity into 12 subtypes and each eye underwent one or more imaging sessions at multiple follow-up timepoints (ETDRS score may change at different follow-up scans).

All OCT and OCTA scans were acquired by a commercial spectral domain OCT system (Avanti RTVue-XR, Optovue, Inc.). The light spectrum is centered at 840 nm with a full-width half-maximum bandwidth of 45 nm. The optical resolution in retina tissue is 5  $\mu\text{m}$  and 15  $\mu\text{m}$  in the axial and lateral directions, respectively. It covers a 3-mm imaging depth and provides a

**Table 1. Participant statistics<sup>a</sup>**

Participants		Subject (N)	Eye (N)	Scan (N)	Age	SSI
Healthy Control Subjects		48	48	48	52.0 ± 15.5	72 ± 7
Diabetes	0: Healthy subjects	55	76	180	47.6 ± 17.4	77 ± 8
	10: DR absent	55	58	148	62.0 ± 13.1	66 ± 8
	15: DR questionable	2	2	5	51.6 ± 21.4	72 ± 2
	20: Microaneurysms only	10	11	26	52.6 ± 12.8	69 ± 12
	35: Mild NPDR	49	50	144	65.9 ± 8.7	63 ± 9
	43: Moderate NPDR	15	16	42	68.0 ± 7.1	61 ± 8
	47: Moderately severe NPDR	18	18	53	60.8 ± 10.5	62 ± 7
	53: Severe NPDR	53	57	150	59.2 ± 11.0	61 ± 8
	61: Mild PDR	49	52	155	54.9 ± 13.8	63 ± 8
	65: Moderate PDR	32	35	103	51.0 ± 10.0	66 ± 8
	71: High-risk PDR I	14	15	53	56.5 ± 13.1	61 ± 9
	75: High-risk PDR II	5	5	10	46.0 ± 20.8	57 ± 4
Subtotal:		325	374	1069	59.1 ± 12.6	66 ± 10
Retinal Artery Occlusion (RAO)		19	19	19	53.9 ± 14.6	57 ± 8
Age-related Macular Degeneration (AMD)		142	280	431	76.9 ± 8.5	57 ± 11

<sup>a</sup>DR: diabetic retinopathy; NPDR: Non-proliferative DR; PDR: proliferative DR; SSI: signal strength index.

3-μm digital sampling interval in the axial direction. The system operates in a 70-kHz A-line scanning rate with a 750 μW exposure power at the pupil.

ILM and BM boundaries were exported from the OCT system, which were calculated automatically using a directional graph search method [21], and manually corrected for errors. Compared to other boundaries, the ILM and BM are the easiest to segment, and generally require minimal manual corrections. In our case, manual corrections were involved in only several scans with very poor (SSI < 45) image quality or regions with severe shadows. Depth in this study was measured as the percent depth to these two boundaries (ILM = 0%; BM = 100%).

## 2.2. Scan registration in different subjects

This innovative algorithm involved a two-step strategy, including the lateral alignment and depth normalization in the axial direction (Fig. 1), to achieve the volumetric registration of scans in different subjects. As the foveal avascular zone (FAZ) [9] is the most obvious feature in macular scans, we used it to perform the lateral alignment, i.e. placing the FAZ to the exact center of a 9×9-mm image. The temporal raphe, part of the boundary between the superior and inferior hemispheres, was almost horizontal in all images, so no image rotations were needed to align the scans. Therefore, the lateral alignment was completed by detecting the center of the FAZ and then rigidly shifting the image to place the center of FAZ to the center of the image.

Here, we proposed an automated method to locate the FAZ center without delineating the accurate boundary in case it was unavailable. This involved 1) applying a gaussian filter (window size: 35×35) to the angiographic *en face* images, 2) inverting the contrast, 3) multiplying it by an image-centered gaussian weight map as the FAZ has a high probability in the center of the image, and 4) locating the FAZ center as the magnitude centroid of the final image (Fig. 2). The 59-μm median distance was obtained from the automatically detected FAZ center to a manually labeled FAZ center for the scans used in this study. After that, foveal center alignment was performed by

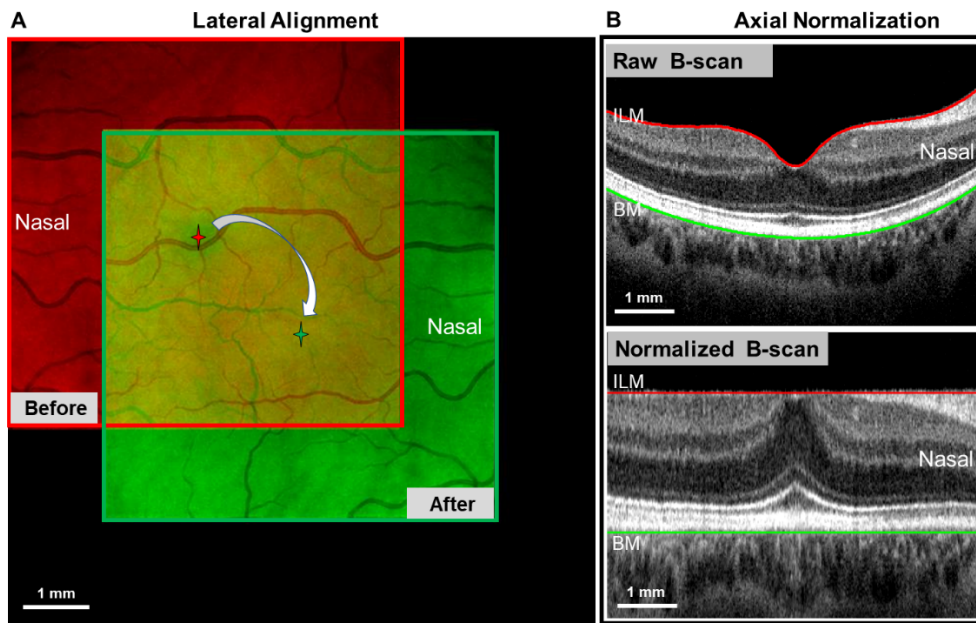


**Fig. 1.** Demonstration of OCT scan registration in different subjects. (A) Lateral registration was achieved by foveal center alignment in a  $9 \times 9$ -mm image, with the nasal side flipped in the left eyes to match with the right eyes. (B) Axial registration is achieved by axially normalizing the A-lines according to percent retinal depth.

moving the FAZ centers to the center of a reference image in a zero-padded matrix, with the nasal and temporal sides flipped in left eyes to match the orientation in right eyes (Fig. 1 A).

Next, axial normalization (ILM:0, BM:100) was performed to eliminate inter-subject variation in retinal thickness. This was achieved by 1) placing the ILM and BM boundaries at fixed depths ( $d_1, d_2$ ), where  $d_1, d_2$  can be constant over the entire retinal regions, or be dependent upon maps to retinal regions as long as the process is kept the same for all scans, 2) calculating the new depth for retinal tissue at Z depth, and 3) interpolating the original A-lines according to the new depth to obtain the normalized A-lines (Fig. 1 B, Eq. (1)). It should be noted that the process leads to heterogeneous axial resolution at different locations. In this study, to preserve the natural appearance of the retina on cross-sectional scans familiar to clinicians and researchers, we placed the BM at a constant depth  $d_2$ , while the ILM was placed at a region-dependent depth, which was determined by the mean retinal thickness maps in healthy subjects, i.e., the BM boundary was flat, and ILM boundary was curved (See figures in Results).

$$\begin{cases} ILM_{x,y} & \rightarrow & d_1 \\ Z_{x,y} & \rightarrow & (Z_{x,y} - ILM_{x,y}) * (d_2 - d_1) / (BM_{x,y} - ILM_{x,y}) + d_1 \\ BM_{x,y} & \rightarrow & d_2 \end{cases} \quad (1)$$

### 2.3. Voxel-wise pathology detection

By registering and merging the scans in healthy subjects, we obtained standard retina volumes, including structural, angiographic, and perfusion (See Sect. 2.4) volumes. These standard retina volumes were further used as references for voxel-wise comparison to detect pathologies by registering the scans from diseased retinas as described above.

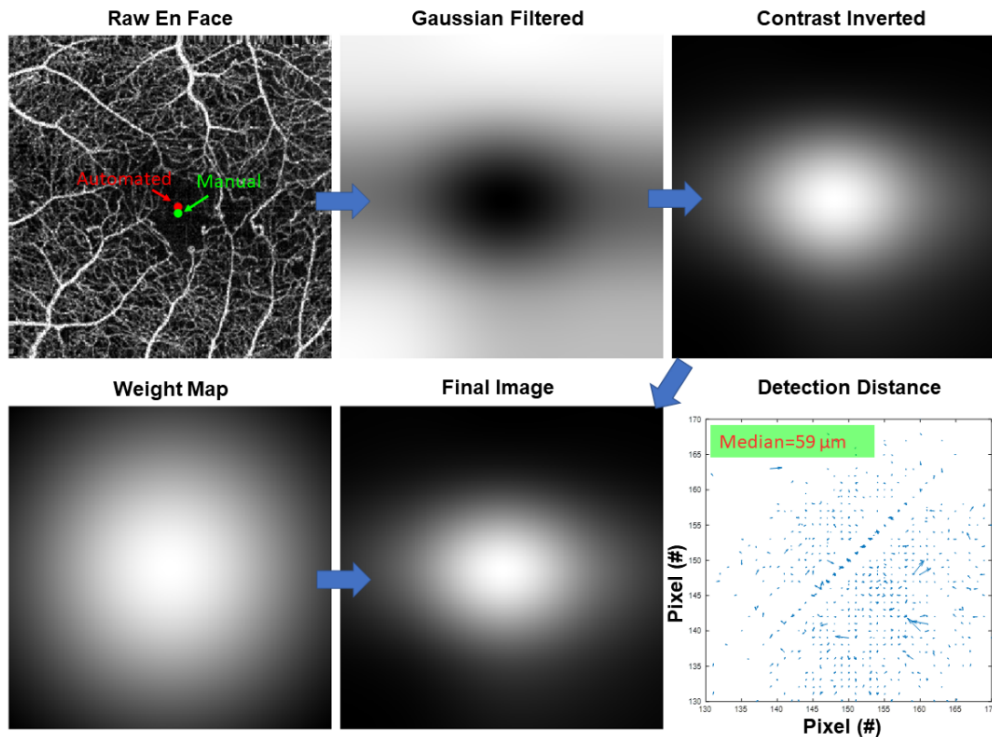


**Fig. 2.** Demonstration of automated detection of FAZ center showing the raw angiographic *en face* image, gaussian filtered, contrast inverted, and final images, as well as the weight map for the localization. The distance of the automated detected and manually labeled FAZ center was calculated with a median distance of 59  $\mu\text{m}$  and all points displayed with MATLAB function *quiver()*.

It was essential to consider the variation of signal strength index (SSI) in the scans to compare the scans fairly, as SSI affected the OCT reflectance values as well as the angiogram values. Previously, it was difficult to eliminate the effect of SSI in the scans as image illumination was non-uniform. Here, by taking advantage of the standard retinas, we proposed a post-registration method to effectively compensate the SSI volumetrically. This was achieved by 1) 3-D filtering (down-sampling followed by up-sampling with a factor of 10 $\times$ ) the reflectance of the scans and standardized retina, 2) calculating the 3-D reflectance ratio map for the filtered scan to the filtered standard retina, and 3) dividing the original scan by the ratio map. After that, the reflectance in the scan was brought to the same level as the standard retina in all regions. It should be noted that due to shadow artifacts from vessels and hard exudates, the hypo-reflectance was overestimated. To correct this, it was necessary to further adjust the structural volume when measuring hypo-reflectance. This was achieved by 1) projecting the structural *en face* image from a slab with upper and lower borders at 20- $\mu\text{m}$  above the BM and the BM for the sample volume and standard volume, 2) calculating the reflectance ratio map of the two *en face* images, and 3) dividing the sample volume by the ratio map.

The pathology  $p$  was detected by the extent to which the scan from the diseased retina ( $x_d$ ) deviated from the reference retina ( $x_r$ ) through voxel-wise comparison, which was calculated from Eq. (2). Unless otherwise noted, the comparison method was the same for the quantification of thickness, reflectance, angiographic and perfusion volumes. The mean magnitude of pathology was calculated as the mean value of pathology volume  $p$  within the volumetric retinal tissue

range. For better visualization, the pathologies were color-coded by both their amplitude and their percent retinal depth at specific voxels.

$$p = \frac{(x_d - x_r)^2}{x_d^2 + x_r^2} \quad (2)$$

#### 2.4. 3-D nonperfusion map

It is known that neuronal retina tissue is supported by blood perfusion from the retinal and choroidal circulation. Several features are anticipated to influence the amount of perfusion from a vessel to a specific location: 1) perfusion is a three-dimensional process; 2) a capillary has maximal perfusion capability at its original location; and 3) perfusion capability decreases with increasing distance. Based on these features, we proposed to model the perfusion capability from a vascular voxel as a 3-D Gaussian kernel  $c = \exp(-r^2/2/\sigma^2)$ , with  $c$  standing for perfusion capability,  $r$  for perfusion distance, and  $\sigma$  for the standard deviation of the Gaussian kernel (Fig. 3). We determined the value of  $\sigma$  as  $40\text{ }\mu\text{m}$  based on the three-sigma rule by considering the  $\sim 120\text{-}\mu\text{m}$  thickness of the avascular outer retina in humans (measured from the healthy subjects in this study) [22], meaning perfusion capability can be neglected beyond that range.

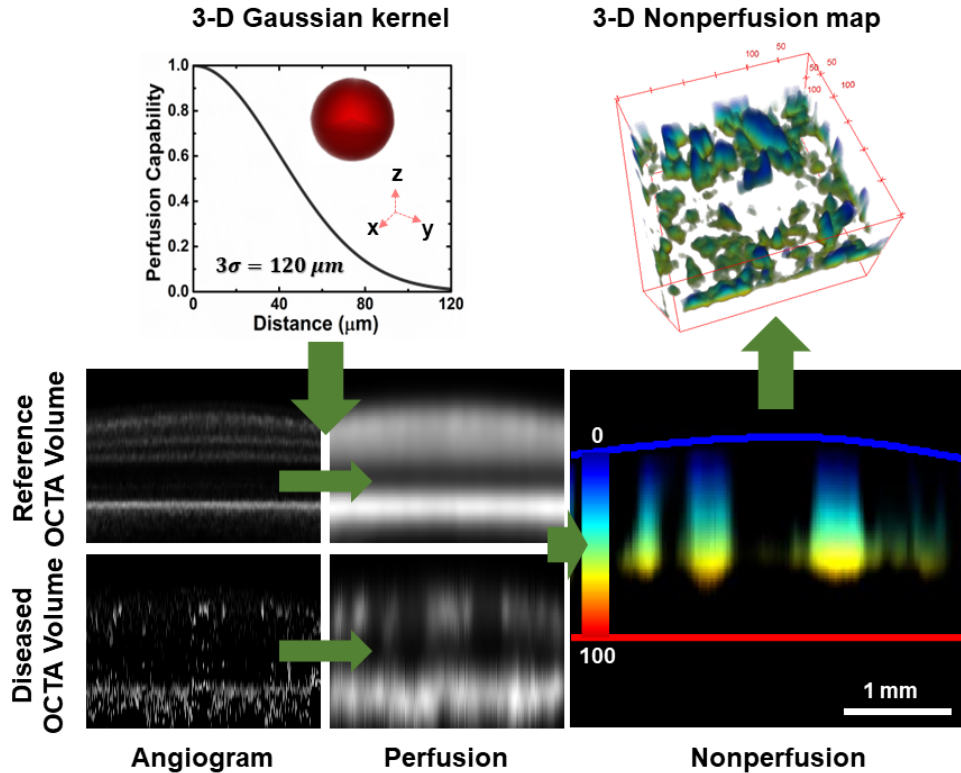


**Fig. 3.** Demonstration of 3-D detection of nonperfusion. The perfusion volume simulated by convoluting the angiogram volume with 3-D Gaussian kernel, and then compared between reference and diseased retinas using Eq. (2) to calculate the 3-D nonperfusion map. The 3-D nonperfusion map is color-coded by percent retinal depth (ILM: 0, BM: 100).

It can be assumed that vessels with a greater blood flow can provide stronger perfusion to retinal tissue, and more vascular voxels indicate more powerful perfusion. Based on these points, we simulated the 3-D blood perfusion map ( $Perfusion = A \times C$ ) by performing a convolution to the

3-D perfusion capability kernel  $C$  with the OCT angiography volume  $A$  (Fig. 3). By comparing with reference values in healthy subjects as described in the last section, nonperfusion regions in diseased retinas were detected in those voxels with values smaller than the reference, with the degree of nonperfusion quantified by Eq. (2) to evaluate how much it deviated from a healthy status.

### 2.5. Pathologic angiogenesis enhancement

In OCTA, projection artifacts in posterior layers can hinder visualization of pathologic angiogenesis in the avascular outer retina. A straightforward strategy for dealing with this complication is to remove the projection artifacts and clean up the outer retinal angiogram [23,24]. However, it is usually hard to differentiate the flow signal from new vessels to projection artifacts generated

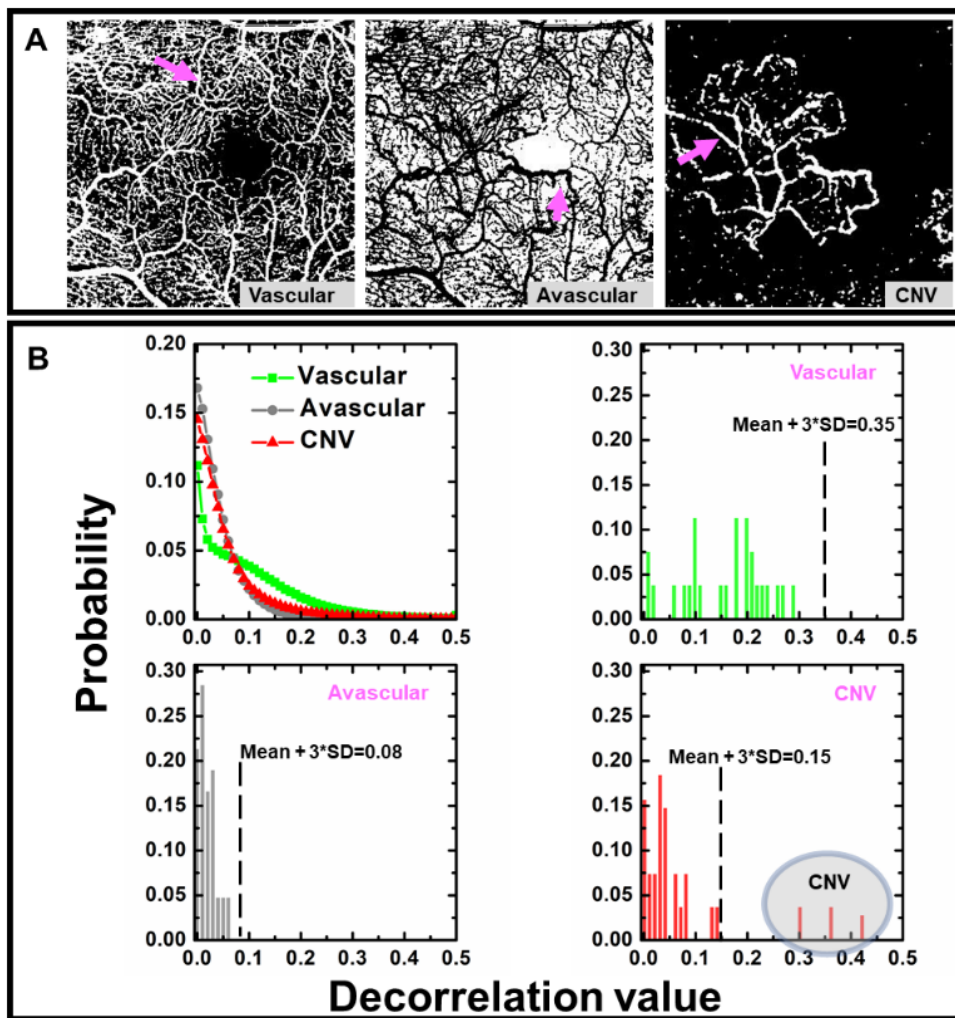


**Fig. 4.** Demonstration of the rationale for the pathologic angiogenesis enhancement algorithm to visualize choroidal neovascularization (CNV). (A) *En face* binary images showing vascular, avascular and CNV A-lines in a scan. (B) The distributions of angiogram decorrelation values for the three types of A-lines over the entire scan and at specific locations (magenta arrows in A).

by anterior vessels. In this study, we demonstrated a simpler approach to distinguish voxels with pathological angiogenesis (for instance, choroidal neovascularization, CNV) in the outer retina from the raw angiogram volume, without removing projection artifacts. The logic of this algorithm is that for each OCTA volume, the A-lines can be categorized into three types: normal vascular A-lines, avascular A-lines, and the A-lines with CNV (Fig. 4 A). For the vascular A-lines, decorrelation values along the depth are largest in the vessel voxels, but also present in layers with strong reflectance. For those layers with weak reflectance, the decorrelation values are minimal and close to 0. This feature causes a bipolar distribution for their decorrelation values in normal vascular A-lines (Fig. 4 B - Vascular). These vascular A-lines have large mean and SD values along the depth. For the avascular A-lines, their decorrelation values are minimal across the entire depth, forming a half-normal distribution centered at 0 (Fig. 4 B - Avascular). These avascular A-lines have small mean and SD values along the depth. However, for the CNV A-lines, the voxels above the CNV are similar to the avascular voxels with the half-normal distribution, and only a few voxels at and posterior to CNV locations have significantly larger decorrelation values. We call this a “disturbed half-normal distribution” (Fig. 4 B - CNV). Therefore, the CNV A-lines have small mean and SD values along the depth, but also outliers at the CNV voxels. The features can be better appreciated in the representative A-lines (Fig. 4 B).

By taking advantage of the distribution of features, a simple approach to identify the CNV voxels is to threshold each A-line using angiogram cutoffs (mean+3×SD) calculated from individual A-lines. For the vascular A-lines, the threshold is very large (0.35 for the representative A-line in Fig. 4 B). For the avascular A-lines, the threshold is small (0.08 for the representative A-line in Fig. 4 B). The decorrelation values of all voxels in those two types of A-lines are below the mean+3×SD threshold. However, the CNV voxels behave as outliers, superior to the thresholds, and thus can be identified in the raw angiogram volume.

### 3. Results

#### 3.1. Standard retina

To obtain the standard retina (Fig. 5 A) used in this work, structural OCT and OCTA volumes from healthy volunteers (Age:  $52.0 \pm 15.5$ , [27 78]) were registered volumetrically by laterally aligning the foveal center and axially normalizing each A-line to percent retinal depth (ILM: 0, BM: 100). Transforming to depth normalized coordinates helped eliminate inherent variation in retinal thickness (Fig. 5 B) and curvature that would otherwise lead to blurry images carrying imprecise anatomic information. Registered in this way, the contrast between retinal layers and vessels in the structural and angiography OCT channels were enhanced instead (Fig. 5 C). In the standard retina, the horizontal raphe is clearly visible in volumetric visualization (Fig. 5 A), indicating morphology can be dramatically enhanced by registering the normal controls in a standard volume. The percent retinal depth maps of all the retinal layers (Fig. 5 D) could also be obtained in this way. Since the percent depth of retinal features is more consistent across healthy populations than the absolute depth, percent retinal depth maps may represent more fundamental and calibrated characteristics of retinas than layer thickness maps.

The retinal laminar vascular / capillary plexuses – including the superficial vascular complex (SVC), intermediate capillary plexus (ICP), and deep capillary (DCP) - can also be differentiated in the merged angiographic volume. In addition, both the merged structural and angiographic standard retinas can be interpreted as probability maps, with the structural volume yielding the probability that a region is highly reflective and the angiographic standard giving the probability that a region is vascularized. However, while the standard structural retina retains the appearance of a scan from a single individual, the standard angiographic retina does not, since blood vessel morphology is unique for each individual. Instead, the SVC, ICP and DCP [25] look like bands, rather than a collection of vessels (Fig. 5 A). This interpretation is corroborated by the location of the strongest flow signal in the choroid, which is known to be a fully vascularized tissue, as well

as the nerve fiber layer plexus (NFLP) visualized in the nasal region. The angiographic standard retina volume does, however, correspond closely to a voxel-wise 3D vessel density map (Fig. 5 E), which was calculated by statistical analysis among different subjects, instead of traditionally within certain regions (e.g. super-pixels).

### 3.2. Pathologies with abnormal reflectivity

An interpretation of the standard retina as a probability map indicates that those regions in a target scan deviating significantly from the standard can be abnormal, and possibly pathological. To enhance visualization of such pathologies, we constructed a deviation image in which the magnitude of voxels gives the degree to which the target scan differs from the standard retina, and the color indicates percent depth. Using this approach, we were able to identify and clearly visualize several important pathologies. For example, PAMM [26,27], which is defined as tissue

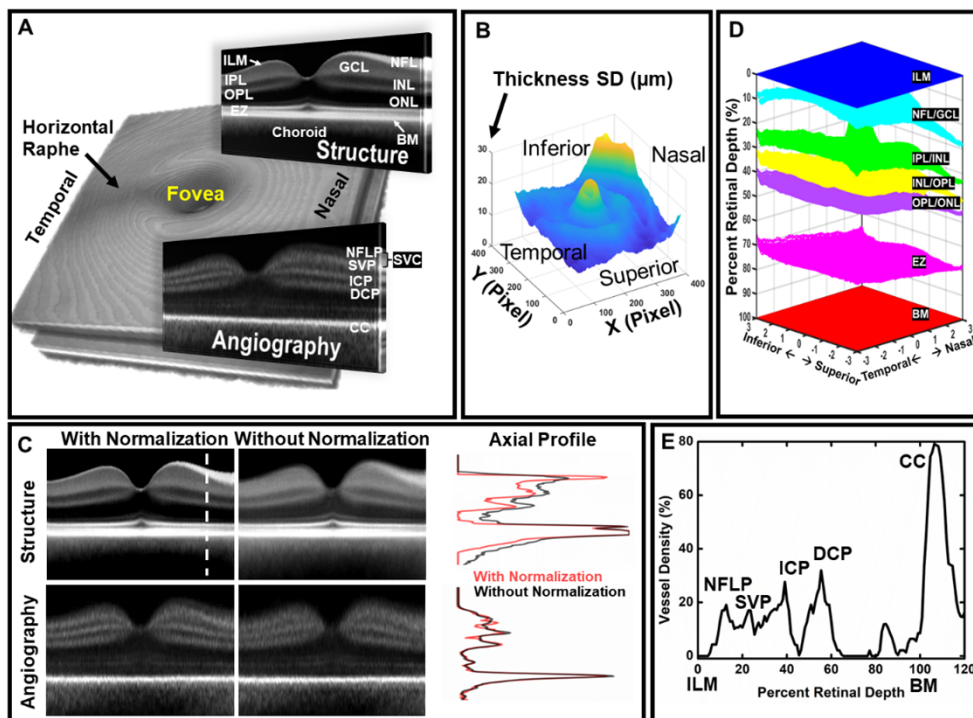


**Fig. 5.** (A) Standard retinal volumes registered and averaged from 48 healthy subjects with representative cross-sectional structural (upper-right corner) and angiographic (lower-right corner) B-scans. (B) Population variation of retinal thickness map. (C) Comparison of a merged retina with and without axial normalization, with axial profiles shown at the location of the dashed white line in the B-scan. The different retinal layers are more readily identifiable with normalization, and layer boundaries are sharper. (D) Percent retinal depth maps for retinal layer boundaries in the macular region (6×6-mm centered at foveal pit) in healthy subjects. (E) Voxel-wise vessel density map demonstrated on an axial profile at the location of the white dashed line in B. ILM: inner limiting membrane, NFL: nerve fiber layer, GCL: ganglion cell layer, IPL: inner plexiform layer, INL: inner nuclear layer, OPL: outer plexiform layer, ONL: outer nuclear layer, EZ: ellipsoid zone, BM: Bruch's membrane, NFLP: nerve fiber layer plexus, SVP: superficial vascular plexus, SVC: superficial vascular complex, ICP: intermediate capillary plexus, DCP: deep capillary plexus, CC: choroid capillary.

with hyper-reflectance in INL, can be easily recognized with this approach (Fig. 6). Compared to the structural *en face* image generated from the single INL slab by an accurate layer boundary segmentation (which involves manual correction), our approach delineated the exact same PAMM location (with INL segmentation waived). We validated pathology detection in the deviation image by measuring the degree to which PAMM co-occurred at the same location in typical structural OCT imaging (Jaccard similarity coefficient [17] = $0.85 \pm 0.08$  in  $n = 19$  eyes with retinal artery occlusions; ground truth determined by thresholding with manual correction). Other pathologies, such as hard exudates [28] in diabetic retinopathy (DR) and drusen [29] in age-related macular degeneration (AMD) are also visually enhanced by the deviation image (Fig. 6). Furthermore, by color-coding the percent retinal depth, our approach can visually depth-resolve pathologies for instance, the extension of PAMM into the ganglion cell complex (GCC), which is otherwise difficult to see in the structural images. For any of these features, the ILM and BM are the only boundaries needed for the visualization.

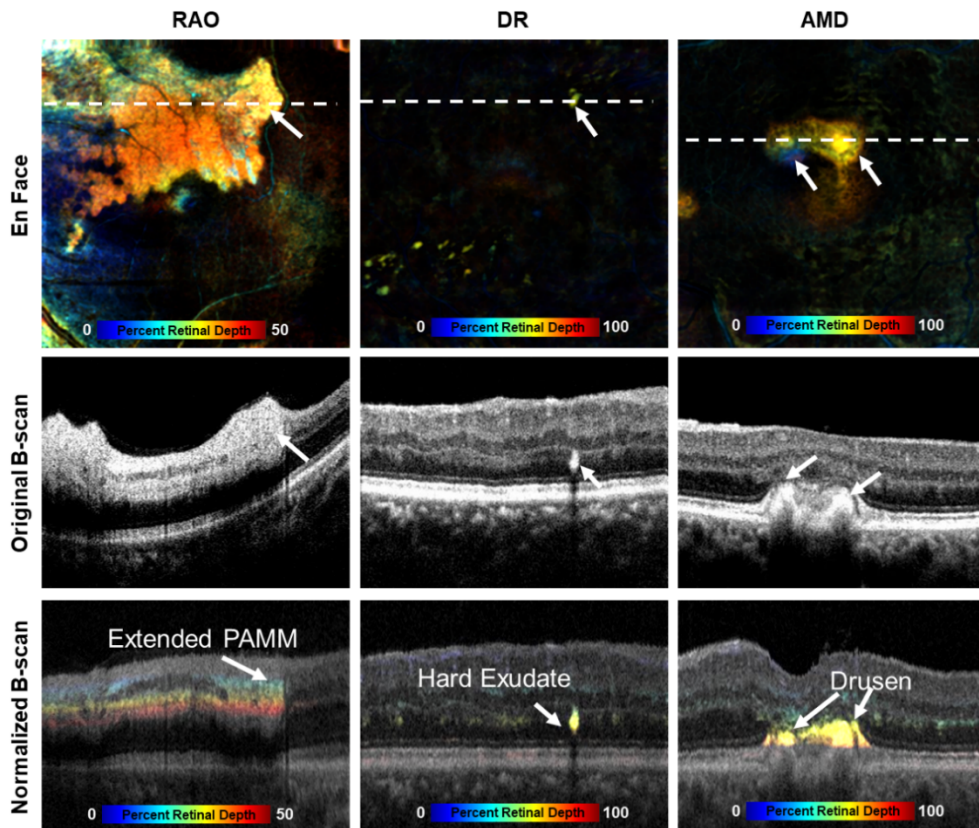


**Fig. 6.** Detection of hyper-reflective retinal pathologies including extended paracentral acute middle maculopathy (PAMM) in retinal artery occlusion (RAO), hard exudates in diabetic retinopathy, and drusen in age-related macular degeneration (AMD), respectively. Colors were coded by percent retinal depth in the B-scans and projected by center of mass for *en face* display.

Hypo-reflective lesions such as retinal fluid [30,31] can also be detected through the proposed framework (Fig. 7). Because shadows from media opacities can artifactually reduce reflectivity, a shadow suppression method was developed. Our framework can easily differentiate various types of retinal fluid (intraretinal, subretinal) where the subretinal fluid can be easily missed by

the conventional mean projection method to generate *en face* images (Fig. 7 B). Our approach also avoids artifacts due to retinal layer mis-segmentations (which are common in retinas with fluid) from producing inaccurate fluid regions.

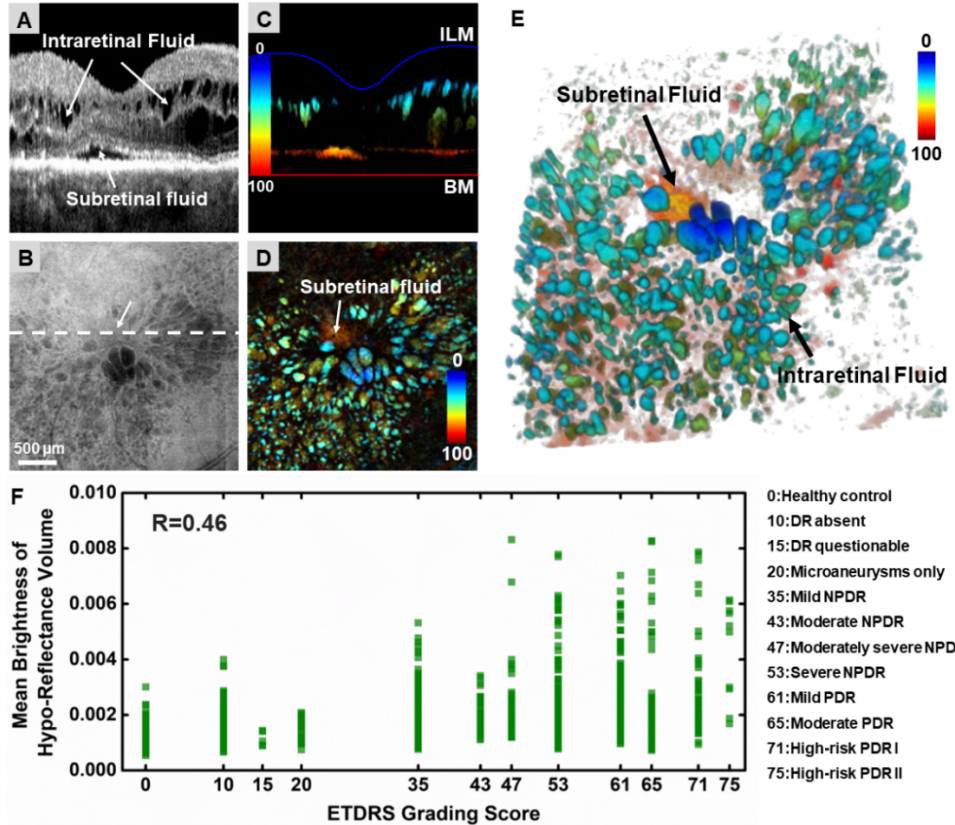


**Fig. 7.** Detection of hypo-reflective retinal fluid in eyes with diabetic retinopathy (DR). (A) Structural B-scan. (B) The structural *en face* image projected from the entire retinal volume. The white line indicates the position of the B-scans in A and C. (C) B-scan, (D) *en face* image, and (E) volume of hypo-reflectance pathology color-coded by percent retinal depth (ILM:0, BM:100). (F) the correlation of mean magnitude of the detected hypo-reflectance with early treatment of diabetic retinopathy study (ETDRS) grading score in a DR dataset with  $n = 1069$  OCT scans. The Spearman correlation coefficient ( $R$ ) was 0.46.

In addition to visualizing these regions, we defined the hypo-reflectivity deviation volume as a biomarker. The mean magnitude of the deviation volume, mainly representing contribution from retinal fluid, correlated with DR severity in 1069 scans (Spearman correlation to Early Treatment of Diabetic Retinopathy Study (ETDRS) score =0.46 ( $p$ -value < 0.01); Fig. 7 F). This metric, the average value of the hypo-reflectance deviation image, does not require segmentation or quantification of any pathologic features, and so represents a conceptually simple and easy-to-use approach to quantifying pathology.

### 3.3. 3-D nonperfusion map

The ability of a vessel to perfuse a location depends on distance. We modeled the vessel perfusion as a 3-D Gaussian kernel and convolved this kernel with the angiographic volumes to simulate the 3-D perfusion volume (Fig. 3). Retinal large vessels were not excluded for simulation due to

the challenges in accurately and automatically segmenting retinal vessels in 3-D. As indicated in Fig. 8, the deviation map between the standard retina and the diseased retina highlights areas of nonperfusion. The correspondence between the detected nonperfusion regions in the deviation image with no flow signal regions in standard OCTA was verified by inspecting B-scans and *en face* images (Fig. 8). As the 3-D nonperfusion was depth-dependent along the A-lines, it was detected only in the inner retina and the ONL but not in the EZ and RPE slabs for the affected A-lines owing to the healthy choroid circulation for this subject. When projecting into the *en face* images, the detected nonperfusion was smaller than the avascular A-line area since blood supply can perfuse beyond the vessel lumens so that a great portion of avascular retinal tissue can have sufficient perfusion. However, nonperfusion region is the region not functionally perfused, which is not identical to the avascular region defined as the lack of blood vessels morphologically/physically. For instance, in the region marked with the white arrow in Fig. 8, the nonperfusion was detected in the OPL slab while the blood vessels in that region still exist in both the superficial and deep retinal vascular plexuses but are sparse and have lower decorrelation values. Similar to hypo-reflective pathology, the mean magnitude of the 3-D retinal nonperfusion deviation volume achieved a Spearman correlation coefficient of 0.61 ( $p$ -value <0.01) with the ETDRS score for the subjects in the same  $n = 1069$  OCT scans.

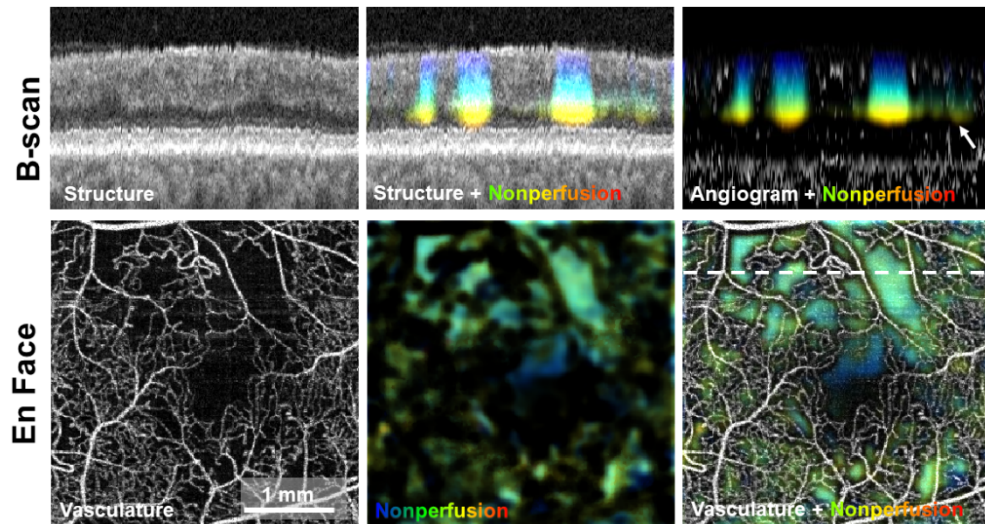


**Fig. 8.** Representative retinal structure, vasculature, detected nonperfusion, and overlays in B-scan and *en face* images. The 3-D nonperfusion map corresponds well with the capillary drop-out in this eye with diabetic retinopathy; however nonperfusion also presented in regions (marked with the white arrow) where the capillaries still exist but were sparse and with lower decorrelation values.

### 3.4. Choroidal neovascularization

Since OCTA projection artifacts cast by anterior retinal circulation were removed by the projection-resolved OCTA (PR-OCTA) algorithm in this work, pathologic angiogenesis such as choroidal neovascularization (CNV) could be detected by comparing the target angiographic volume with the standard angiographic volume, with color indicating the CNV depth. In this comparison, the standard angiographic volume acted as a 3-D threshold map to identify the vascular voxels from both the normal circulation and pathologic angiogenesis.

However, CNV is usually observed in the outer retina, which is avascular in healthy eyes. Due to its posterior location, CNV produces fewer projection artifacts than the normal retinal vessels

without projection artifacts removal. Consequently, the distributions of the raw angiographic decorrelation value along the depth for each A-line can be categorized into three types: a half-normal distribution for avascular A-lines, a bipolar distribution for vascular A-lines, and a “disturbed half-normal” distribution for CNV A-lines (Fig. 4). Here, by setting thresholds (Mean+3×SD) for the angiogram of each A-line, we developed a pathologic angiogenesis enhancement (PAE) algorithm to distinguish CNV voxels from raw OCTA volume (Fig. 9). The PAE angiographic volume could also be projected to a depth-coded *en face* image, which had comparable CNV visualization to an *en face* image made using PR-OCTA (Fig. 9 F).

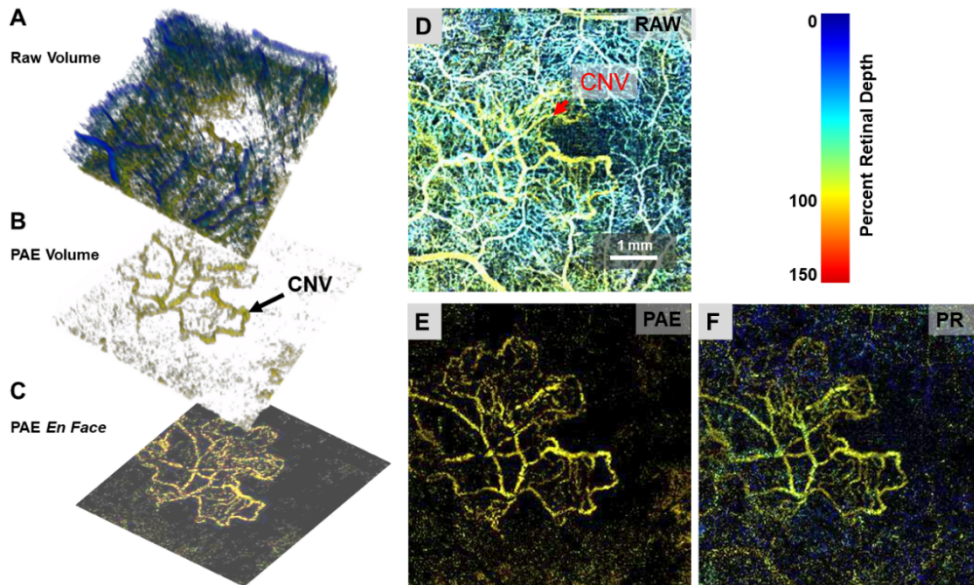


**Fig. 9.** Visualization of CNV in an eye with age-related macular degeneration (AMD) detected with the pathologic angiogenesis enhancement (PAE) algorithm. (A) Volumetric visualization of the raw angiogram. (B) Volumetric visualization of pathological angiogenesis enhanced (PAE) angiogram revealing CNV. (C) *En face* visualization of the PAE angiogram delineating the CNV. (D-F) *En face* visualization of CNV processed with (D) raw angiograms, (E) the proposed PAE algorithm, compared to (F) projection resolved (PR) algorithm. The scale bar was extended into the choroid as the CNV originated.

### 3.5. Pathology index

In cases of retinal tissue loss, such as in glaucoma or geographic atrophy, the retinal thickness will change. Therefore a 2-D retinal thickness change analysis can be calculated similarly to obtain deviation from healthy subjects and to detect tissue loss. In addition, the location (depth) of the retinal tissue loss may be observed in the hyper- or hypo- reflectance detection. We constructed a biomarker called pathology index for each scan based on the magnitude of the deviation values. Instead of focusing on the quantification of a specific clinical feature, this framework was based on principles that could be applied indiscriminately to quantify the hyper-reflectance, hypo-reflectance, nonperfusion, CNV, and retinal thickness change in structural OCT and OCTA images of eyes with multiple diseases. The logic for constructing the pathology index is based on retinal morphologic abnormality (thickness change), reflectance abnormalities (hyper- and hypo- reflectance), and perfusion abnormalities (capillary drop-out and angiogenesis such as CNV). To obtain the reference  $P_h$  for the calculation of the pathology index for each feature, the

magnitude of the deviation values was first averaged within the volume and then averaged within the  $N = 55$  healthy eyes in the DR dataset. After that, the pathology index was calculated as the decibel ratio of the averaged magnitude of deviation values  $P_d$  within the target retinal scan to the reference  $P_h$ , followed by normalization between 0 to 40 dB. The pathology indexes for the five clinical features (hyper-reflectance, hypo-reflectance, nonperfusion, CNV, and retinal thickness change) were then combined as the averaged pathology index for that scan. We tested the utility of the pathology index with a dataset containing 1069 scans of eyes with DR. The Spearman correlation coefficient for the pathology index with DR severity was 0.95 (Fig. 10). In addition, the area under the receiver operating characteristic curve (AROC) for the pathology index to differentiate referable DR from non-referable DR cases was 0.87. The low AROC for the CNV in DR dataset can be anticipated since CNV is not a common feature seen in DR. Preretinal neovascularization may need to be included to fairly evaluate pathological angiogenesis in DR. The current cut-off pathology index of 6 was obtained with the optimal diagnostic strategy for referable and non-referable DR. Here we demonstrated the usefulness of pathology index only in DR since the ETDRS score [20] is a well-accepted grading system to characterize the DR severity while similar grading systems lack for other diseases. A universal cut-off value for screening all retinal diseases would deserve more detailed studies though.

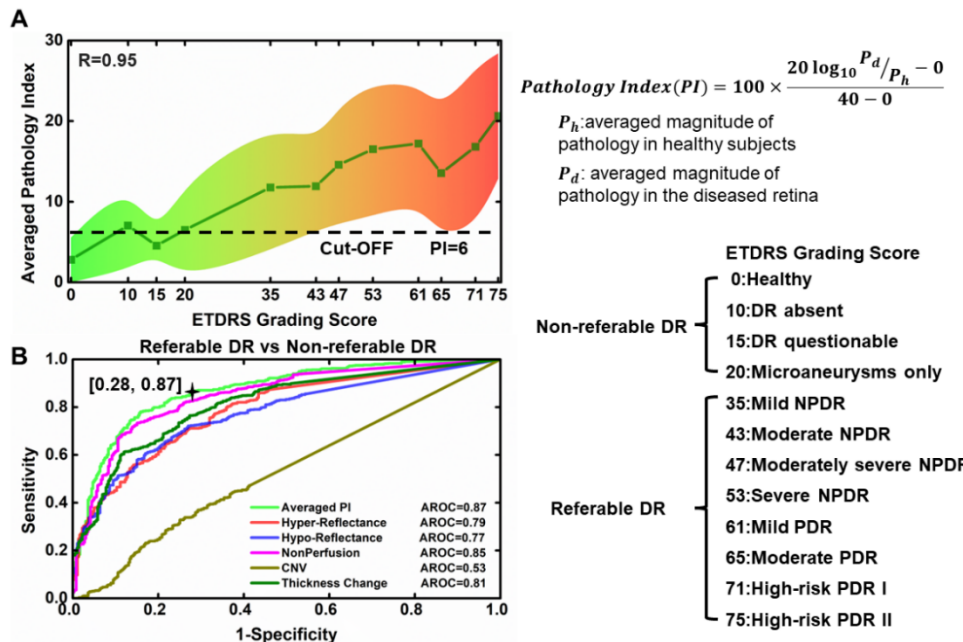


**Fig. 10.** Diagnostic power of various pathology indexes to differentiate non-referable DR from referable DR subjects. The pathology index for each clinical feature was calculated as the decibel ratio of the averaged deviation magnitude from a target retinal scan ( $P_d$ ) to baselines ( $P_h$ ) from healthy subjects. (A) The combined pathology index achieved an  $R = 0.95$  Spearman correlation coefficient with the DR severity. The black dotted line indicates a pathology index cut-off  $PI = 6$  corresponding to the best diagnostic point in B. (B) Receiver operating characteristic curves for the pathology indexes of each clinical feature, and the combined one for referable vs. non-referable DR classification. The optimal operating point of the ROC curve for the averaged PI was determined as 1-specificity = 0.28 and sensitivity = 0.87, output from the parameter *OPTROCPT* of the MATLAB function *perfcurve()*.

#### 4. Discussion

OCT and OCTA provide micron-resolution volumetric data sets. Currently, interpretation of OCT and OCTA scans rely on 2D images such as *en face* slab projections or cross-sections due to the lack of an effective 3D analytic framework. Several challenges impede the development of such a framework: (1) Significant population variation exists in retinal measurements [32]. For example, OCT retinal thickness measurements have low sensitivity and specificity to detect diabetic retinopathy [33]. (2) The reflectance signal that OCT relies on to generate tissue contrast can be influenced by opacities that affect the illumination pathway. This can cause variations in signal strength from scan to scan, and even region to region, which complicates analysis. (3) Current OCT/OCTA volumetric analyses are difficult to verify due to difficulties displaying volumetric data. This is problematic, as clinicians may need to correlate the output with clinical findings.

In this study, we demonstrated a conceptually simple framework for processing volumetric structural OCT and OCTA that can aid in disease detection and visualization of retinal pathologies. This framework relies on the construction of standard retinas by merging depth-normalized scans from healthy subjects. As we showed in the results, a voxel-wise comparison between a target retina and the standard retina volumes for structure, angiography, and simulated 3D perfusion map can reveal pathology. Normalizing the depth between the ILM and BM reduces the effect of population variation in retinal thickness, which can confound disease detection [34,35]. Normalization by depth also enables consistent color-mapping that can accurately locate pathology in 3 dimensions. In this way, intraretinal and subretinal fluid can be more easily differentiated, which is important since different fluid locations influence treatment response in diabetic macular edema [36]. Additionally, we showed that a disease agnostic pathology index generated from this framework correlated with DR severity, indicating that this approach could also provide quantitative diagnostic value. The innovative algorithms proposed in this study are summarized in Table 2.

**Table 2. Summary of proposed algorithms**

Algorithm	Description
Scan Registration	<b>Detection of FAZ center</b> The centroid of image with Gaussian filtering and other operations
	<b>FAZ alignment</b> Place the FAZ in the center of the image
	<b>Percent depth normalization</b> Reconstruct retina with respect to ILM and BM boundaries
Voxel-wise pathology detection	<b>Merge for standard retina</b> Average registered and normalized scans from healthy subjects
	<b>SSI compensation</b> Normalize to the 3-D landscape of the reference standard retina
	<b>Shadow artifacts compensation</b> Normalize based on RPE slab for hypo-reflectance detection
	<b>Deviation volume calculation</b> Voxel-wise comparisons of reflectance, angiography, and perfusion
	<b>Percent depth color-coding</b> Assign colors to the voxels based on their percent retinal depths
<b>Simulation of 3-D blood perfusion map</b> Convolute OCTA with 3-D perfusion capability kernel	
<b>Pathological angiogenesis enhancement</b> Threshold voxels based on distribution of angiogram in A-lines	
<b>Calculation of pathology index</b> Normalized decibel ratio (target retina / healthy subjects)	

The proposed framework has three significant advantages. First, it is volume-based and is performed directly on volumetric scans. We have previously reported that 3D vessel density demonstrated foveal ischemia more effectively than 2D methods [17], and 3D retinal fluid can provide more comprehensive information than the 2D area [16]. Second, it is layer-independent, requiring just the ILM and BM borders. As these are the most accessible boundaries to identify, this approach avoids errors that can arise during the segmentation of multiple retinal layers. Third, it can cover a wide spectrum of clinical features. It is generally not easy to appreciate

volume data. The major point of color-coding the deviation is to retain the depth information when projecting the volume into the *en face* images for demonstration. It would be extremely useful to differentiate the pathologies from different depths (a good example is Fig. 7 D) without requirements to segment specific slabs. The percent retinal color-coding proposed in this study doesn't conflict with other approaches to highlight the pathological regions.

Future work could expand on our current results. First, with the ability to detect changes in both morphology (hyper-reflectance, hypo-reflectance, retinal thickness) and function (nonperfusion and CNV), we explored the possibility of establishing a pathology index. Although only investigated here in the context of DR, we believe that this index could have clinical significance in a range of retinal diseases, such as retinal vein occlusion or age-related macular degeneration, since the features used to construct the index are not specific to DR. Second, we constructed our standard retina using data from 48 healthy individuals, which represented a range of demographics. It is possible that we could improve the sensitivity for pathology detection if, instead of a single generic standard, we developed multiple standard volumes that reflected specific demographic characteristics such as age, sex, and ethnicity. Thirdly, we are aware of the limitation caused by simulating perfusion using a gaussian kernel. In the following studies, we will take the diffusion process and retinal layer-specific metabolism into consideration from the perspective of physiology to further improve it and explore its usefulness. Finally, while the framework was demonstrated in macular scans, the same approach could be adapted for other regions, such as the optic disc.

In summary, we established a 3D analytic framework to detect retinal pathologies with commercial OCT and OCTA by enabling volumetric comparisons of OCT scans from different subjects, with color-coding by normalized depth in order to better appreciate the pathologies in projected *en face* images. The biomarker from the identified pathologies correlated well with DR severity. Features from a number of diseases other than DR were clearly visualized with this framework. We believe that this disease-agnostic, 3-D approach can enhance disease detection and analysis if integrated into commercial OCT/OCTA systems.

**Funding.** BrightFocus Foundation (G2020168); Knights Templar Eye Foundation; Research to Prevent Blindness; National Institutes of Health (P30 EY010572, R01 EY010145, R01 EY024544, R01 EY027833, R01 EY031394, R01 EY023285, T32 EY023211, UL1TR002369).

**Disclosures.** Oregon Health & Science University (OHSU), Dr. David Huang and Dr. Yali Jia have a significant financial interest in Optovue, Inc. These potential conflicts of interest have been reviewed and managed by OHSU. Other authors do not have financial interest to the disclosure of this article.

**Data availability.** Data underlying the results presented in this paper are not publicly available at this time but may be obtained from the authors upon reasonable request.

## References

1. A. P. Schachat, C. P. Wilkinson, D. R. Hinton, P. Wiedemann, K. B. Freund, and D. Sarraf, *Ryan's retina e-book* (Elsevier Health Sciences, 2017).
2. D. Huang, E. A. Swanson, C. P. Lin, J. S. Schuman, W. G. Stinson, W. Chang, M. R. Hee, T. Flotte, K. Gregory, and C. A. Puliafito, "Optical coherence tomography," *Sci.* **254**(5035), 1178–1181 (1991).
3. M. R. Hee, J. A. Izatt, E. A. Swanson, D. Huang, J. S. Schuman, C. P. Lin, C. A. Puliafito, and J. G. Fujimoto, "Optical coherence tomography of the human retina," *Arch. Ophthalmol.* **113**(3), 325–332 (1995).
4. N. Nassif, B. Cense, B. H. Park, S. H. Yun, T. C. Chen, B. E. Bouma, G. J. Tearney, and J. F. de Boer, "In vivo human retinal imaging by ultrahigh-speed spectral domain optical coherence tomography," *Opt. Lett.* **29**(5), 480–482 (2004).
5. B. Lumbroso, D. Huang, E. Souied, and M. Rispoli, *Practical Handbook of OCT Angiography* (JP Medical Ltd, 2016).
6. Y. Jia, S. T. Bailey, T. S. Hwang, S. M. McClintic, S. S. Gao, M. E. Pennesi, C. J. Flaxel, A. K. Lauer, D. J. Wilson, and J. Horngger, "Quantitative optical coherence tomography angiography of vascular abnormalities in the living human eye," *Proc. Natl. Acad. Sci.* **112**(8), 2395–2400 (2015).
7. A. H. Kashani, C.-L. Chen, J. K. Gahm, F. Zheng, G. M. Richter, P. J. Rosenfeld, Y. Shi, and R. K. Wang, "Optical coherence tomography angiography: a comprehensive review of current methods and clinical applications," *Prog. Retinal Eye Res.* **60**, 66–100 (2017).
8. T. Zhang, A. M. Kho, G. Yiu, and V. J. Srinivasan, "Visible light optical coherence tomography (OCT) quantifies subcellular contributions to outer retinal band 4," *Trans. Vis. Sci. Tech.* **10**(3), 30 (2021).

9. T. Y. Chui, D. A. VanNasdale, A. E. Elsner, and S. A. Burns, "The association between the foveal avascular zone and retinal thickness," *Invest. Ophthalmol. Visual Sci.* **55**(10), 6870–6877 (2014).
10. J. Campbell, M. Zhang, T. Hwang, S. Bailey, D. Wilson, Y. Jia, and D. Huang, "Detailed vascular anatomy of the human retina by projection-resolved optical coherence tomography angiography," *Sci. Rep.* **7**(1), 42201 (2017).
11. A. Petzold, L. J. Balcer, P. A. Calabresi, F. Costello, T. C. Frohman, E. M. Frohman, E. H. Martinez-Lapiscina, A. J. Green, R. Kardon, and O. Outteryck, "Retinal layer segmentation in multiple sclerosis: a systematic review and meta-analysis," *The Lancet Neurology* **16**(10), 797–812 (2017).
12. Y. Jia, S. T. Bailey, D. J. Wilson, O. Tan, M. L. Klein, C. J. Flaxel, B. Potsaid, J. J. Liu, C. D. Lu, and M. F. Kraus, "Quantitative optical coherence tomography angiography of choroidal neovascularization in age-related macular degeneration," *Ophthalmology* **121**(7), 1435–1444 (2014).
13. R. F. Spaide, J. G. Fujimoto, N. K. Waheed, S. R. Sadda, and G. Staurenghi, "Optical coherence tomography angiography," *Prog. Retinal Eye Res.* **64**, 1–55 (2018).
14. L. Fang, D. Cunefare, C. Wang, R. H. Guymer, S. Li, and S. Farsiu, "Automatic segmentation of nine retinal layer boundaries in OCT images of non-exudative AMD patients using deep learning and graph search," *Biomed. Opt. Express* **8**(5), 2732–2744 (2017).
15. Y. Guo, A. Camino, M. Zhang, J. Wang, D. Huang, T. Hwang, and Y. Jia, "Automated segmentation of retinal layer boundaries and capillary plexuses in wide-field optical coherence tomographic angiography," *Biomed. Opt. Express* **9**(9), 4429–4442 (2018).
16. Y. Guo, T. T. Hormel, H. Xiong, J. Wang, T. S. Hwang, and Y. Jia, "Automated segmentation of retinal fluid volumes from structural and angiographic optical coherence tomography using deep learning," *Trans. Vis. Sci. Tech.* **9**(2), 54 (2020).
17. B. Wang, A. Camino, S. Pi, Y. Guo, J. Wang, D. Huang, T. S. Hwang, and Y. Jia, "Three-dimensional structural and angiographic evaluation of foveal ischemia in diabetic retinopathy: method and validation," *Biomed. Opt. Express* **10**(7), 3522–3532 (2019).
18. M. N. Menke, S. Dabov, P. Knecht, and V. Sturm, "Reproducibility of retinal thickness measurements in healthy subjects using spectralis optical coherence tomography," *Am. J. Ophthalmol.* **147**(3), 467–472 (2009).
19. M. Wagner-Schuman, A. M. Dubis, R. N. Nordgren, Y. Lei, D. Odell, H. Chiao, E. Weh, W. Fischer, Y. Sulai, and A. Dubra, "Race-and sex-related differences in retinal thickness and foveal pit morphology," *Invest. Ophthalmol. Visual Sci.* **52**(1), 625–634 (2011).
20. E. T. D. R. S. R. Group, "Fundus photographic risk factors for progression of diabetic retinopathy: ETDRS report number 12," *Ophthalmology* **98**(5), 823–833 (1991).
21. M. Zhang, J. Wang, A. D. Pechauer, T. S. Hwang, S. S. Gao, L. Liu, L. Liu, S. T. Bailey, D. J. Wilson, and D. Huang, "Advanced image processing for optical coherence tomographic angiography of macular diseases," *Biomed. Opt. Express* **6**(12), 4661–4675 (2015).
22. S. Areppalli, S. K. Srivastava, M. Hu, P. M. Kaiser, N. Dukles, J. L. Reese, and J. P. Ehlers, "Assessment of inner and outer retinal layer metrics on the Cirrus HD-OCT Platform in normal eyes," *PLoS One* **13**(10), e0203324 (2018).
23. M. Zhang, T. S. Hwang, J. P. Campbell, S. T. Bailey, D. J. Wilson, D. Huang, and Y. Jia, "Projection-resolved optical coherence tomographic angiography," *Biomed. Opt. Express* **7**(3), 816–828 (2016).
24. J. Wang, M. Zhang, T. S. Hwang, S. T. Bailey, D. Huang, D. J. Wilson, and Y. Jia, "Reflectance-based projection-resolved optical coherence tomography angiography," *Biomed. Opt. Express* **8**(3), 1536–1548 (2017).
25. T. T. Hormel, Y. Jia, Y. Jian, T. S. Hwang, S. T. Bailey, M. E. Pennesi, D. J. Wilson, J. C. Morrison, and D. Huang, "Plexus-specific retinal vascular anatomy and pathologies as seen by projection-resolved optical coherence tomographic angiography," *Prog. Retinal Eye Res.* **80**, 100878 (2021).
26. J. Scharf, K. B. Freund, S. Sadda, and D. Sarraf, "Paracentral acute middle maculopathy and the organization of the retinal capillary plexuses," *Prog. Retinal Eye Res.* **81**, 100884 (2021).
27. D. Sarraf, E. Rahimy, A. A. Fawzi, E. Sohn, I. Barbazetto, D. N. Zacks, R. A. Mittra, J. M. Klancnik, S. Mrejen, and N. R. Goldberg, "Paracentral acute middle maculopathy: a new variant of acute macular neuroretinopathy associated with retinal capillary ischemia," *JAMA Ophthalmol.* **131**(10), 1275–1287 (2013).
28. J. Lammer, M. Bolz, B. Baumann, M. Pircher, B. Gerendas, F. Schlanitz, C. K. Hitzenberger, and U. Schmidt-Erfurth, "Detection and analysis of hard exudates by polarization-sensitive optical coherence tomography in patients with diabetic maculopathy," *Invest. Ophthalmol. Visual Sci.* **55**(3), 1564–1571 (2014).
29. R. Zhao, A. Camino, J. Wang, A. M. Hagag, Y. Lu, S. T. Bailey, C. J. Flaxel, T. S. Hwang, D. Huang, and D. Li, "Automated drusen detection in dry age-related macular degeneration by multiple-depth, en face optical coherence tomography," *Biomed. Opt. Express* **8**(11), 5049–5064 (2017).
30. T. Schlegl, S. M. Waldstein, H. Bogunovic, F. Endsträßer, A. Sadeghipour, A.-M. Philip, D. Podkowinski, B. S. Gerendas, G. Langs, and U. Schmidt-Erfurth, "Fully automated detection and quantification of macular fluid in OCT using deep learning," *Ophthalmology* **125**(4), 549–558 (2018).
31. J. Wang, M. Zhang, A. D. Pechauer, L. Liu, T. S. Hwang, D. J. Wilson, D. Li, and Y. Jia, "Automated volumetric segmentation of retinal fluid on optical coherence tomography," *Biomed. Opt. Express* **7**(4), 1577–1589 (2016).
32. A. Chan, J. S. Duker, T. H. Ko, J. G. Fujimoto, and J. S. Schuman, "Normal macular thickness measurements in healthy eyes using Stratus optical coherence tomography," *Arch. Ophthalmol.* **124**(2), 193–198 (2006).

33. M. Afarid, N. Mohsenipoor, H. Parsaei, Y. Amirmoezzi, M. Ghofrani-Jahromi, P. Jafari, A. Mohsenipour, and F. Sanie-Jahromi, "Assessment of macular findings by OCT angiography in patients without clinical signs of diabetic retinopathy: radiomics features for early screening of diabetic retinopathy," *BMC Ophthalmol.* **22**(1), 281 (2022).
34. S. Nunes, I. Pereira, A. Santos, R. Bernardes, and J. Cunha-Vaz, "Retinal thickness with HD-OCT is not a surrogate outcome for visual acuity changes in diabetic macular edema," *Br. J. Ophthalmol.* **94**(9), 1201–1204 (2010).
35. G. Virgili, M. Parravano, J. R. Evans, I. Gordon, and E. Lucenteforte, "Anti-vascular endothelial growth factor for diabetic macular oedema: a network meta-analysis," Cochrane Database of Systematic Reviews (2018).
36. B. S. Gerendas, S. Prager, G. Deak, C. Simader, J. Lammer, S. M. Waldstein, T. Guerin, M. Kundi, and U. M. Schmidt-Erfurth, "Predictive imaging biomarkers relevant for functional and anatomical outcomes during ranibizumab therapy of diabetic macular oedema," *Br. J. Ophthalmol.* **102**(2), 195–203 (2018).